



CrossMark
 click for updates

Cite this: *RSC Adv.*, 2015, 5, 81790

Reactive magnetron sputtered wear resistant multilayer transition metal carbide coatings: microstructure and tribo-mechanical properties†

D. Dinesh Kumar,^{ab} N. Kumar,^{*c} S. Kalaiselvam,^b R. Radhika,^d S. Dash,^c A. K. Tyagi^c and R. Jayavel^a

To enhance the performance and durability of mechanical components, surface properties need to be modified. In this work, a unique combination of transition metal carbide (TMC) multilayer coatings (TiC/CrC, TiC/ZrC and TiC/WC) were deposited by reactive DC magnetron sputtering on 316LN steel substrates. GIXRD results showed the presence of an amorphous CrC phase in the TiC/CrC multilayer, whereas, crystalline TiC, ZrC and W₂C phases were observed in their respective coatings. FESEM analysis indicated the non-columnar structures of TMC layers in all the samples, except the CrC layer in the TiC/CrC multilayer. Solid solutions of the TiC and WC layers at the interface were identified due to the migration of W atoms into the TiC crystal lattices. The poor crystalline nature of the TiC/CrC multilayer led to lower hardness and weak wear resistance. However, enhanced tribo-mechanical properties were observed in TiC/ZrC and TiC/WC multilayer coatings. This is explained by the improved crystallinity and enhanced resistance to plastic deformation. For the selected tribological parameters, abrasive, adhesive and combined abrasive/adhesive wear modes are the major governing factors in determining the wear behaviors of TiC/CrC, TiC/ZrC and TiC/WC coatings, respectively. The chemical stability of deformed wear tracks was observed by Raman spectroscopy.

Received 15th August 2015
 Accepted 21st September 2015

DOI: 10.1039/c5ra16465f

www.rsc.org/advances

1. Introduction

Austenitic 316LN stainless steel is considered as a corrosion resistant, oxidation resistant, and biocompatible material. This is widely used as the ball bearing material in automobile industries, structural materials in fast breeder test reactors, orthopedic implants in biomedical industries and cutting tool industries.^{1–3} To further improve the energy efficiency and durability of the steel surface, nanocrystalline hard coatings are extensively applied.⁴ Such coatings are applicable as diffusion barriers in semiconductor industries, thermal barriers in fusion reactors and wear resistance coatings in moving mechanical components, cutting tools and biomedical implant industries.⁵ Generally, binary transition metal nitride (TMN) and transition metal carbide (TMC) coatings are widely considered from this

perspective, because of their potential properties such as high hardness, low friction coefficient, and good wear and corrosion resistance.^{6,7} Nevertheless, single layer hard coatings fail to meet the strict needs of enhanced performance and life of the mechanical components.⁸ Therefore, a number of studies have been attempted to develop more efficient protective coatings. Multicomponent and multilayer coatings have been developed to meet such technological requirements.^{6,9–11} Among them, the multilayer concept, which is the deposition of alternating layers of different materials, has recently been paid much attention owing to its enhanced mechanical properties.^{11,12} Such enhancements in multilayer coatings compared to the corresponding monoliths, are due to the change in the elastic properties of the sub-layers. From this aspect, a number of transition metal (TM) based multilayer combinations, including metal/metal, metal/ceramics and ceramics/ceramics have been recently investigated.^{11,13–15} It is well-known that carbide coatings possess superior wear resistance properties than nitride coatings due to the presence of the carbon matrix at the grain boundaries of TMC crystallites.¹⁶ These carbons facilitate the grain boundary sliding that introduces ductility and inhibits the nucleation and migration of cracks, resulting in enhanced wear resistance.¹⁷ However, there are no studies available on the microstructure and tribo-mechanical properties of TMC/TMC multilayer systems. In carbide/carbide multilayer systems, the excess carbon matrix over the surface of the base TMC layer could facilitate the

^aCentre for Nanoscience and Technology, Anna University, Chennai 600025, Tamil Nadu, India

^bDepartment of Applied Science and Technology, Anna University, Chennai 600025, Tamil Nadu, India

^cMaterials Science Group, Indira Gandhi Centre for Atomic Research, Kalpakkam 603102, Tamil Nadu, India. E-mail: niranjan@igcar.gov.in; phystribology@gmail.com; Fax: +914427480081; Tel: +914427480081

^dDepartment of Physics, Indian Institute of Technology Madras, Chennai, Tamil Nadu, India

† Electronic supplementary information (ESI) available. See DOI: 10.1039/c5ra16465f

nucleation of another, but different TMC over-layer, resulting in the covalent bonding between sub-layers. Therefore, it is essential to study the properties of TMC/TMC multilayer systems, to obtain novel coatings for better load-bearing capacity. PVD techniques are favoured to deposit such hard multilayer coatings; in particular, magnetron sputtering is an effective tool to fabricate the multilayer owing to its versatility.¹⁸

A novel motivation behind this work was to design the wear resistant coating using the transition metal multilayer concept. For this purpose, systematic TMC multilayer coatings (*i.e.* TiC/CrC, TiC/ZrC and TiC/WC) were deposited on the 316LN steel substrates, using the DC magnetron sputtering technique. The correlation of microstructure and tribo-mechanical characteristics of multilayer samples is established. The wear mode is described to investigate its relationship with wear resistance.

2. Experimental section

2.1 Coatings deposition

The TMC multilayer coatings were deposited on the surface polished 316LN SS substrates with the dimension of $15 \times 10 \times 1$ mm using the reactive DC magnetron sputtering technique. The detailed substrate preparation procedure has been reported elsewhere.¹⁹ The average roughness of the polished substrates was found to be 30 nm. In addition, silicon (100) substrates (10×10 mm) were used to analyze the cross-section and thickness measurements of the TMC multilayer coatings. Highly pure (99.997%) Ti, Cr, Zr and W discs of 50 mm diameter and 3 mm thickness were used as the target materials. These targets were procured from Taewon Scientific Co. Ltd., Korea. The substrates were placed on a movable sample holder, which was fixed perpendicular to the target, at the target-substrate distance of 70 mm. The substrate temperature was kept constant at about 250 °C. The chamber was evacuated up to the base pressure of 9×10^{-6} mbar. The optimized process parameters were used to deposit the multilayer coatings. During the deposition process, Ar (99.999%) gas was fed into the chamber at the constant flow rate of 30 sccm for all the samples, whereas, the CH₄ (99.999%) flow rate was varied as 5 sccm and 8 sccm for the TiC and ZrC, and CrC and WC layers, respectively. The total deposition pressure was maintained at about 2×10^{-3} mbar. Prior to the deposition, all the target surfaces were sputter cleaned for 5 minutes to remove the surface contamination. In order to improve the interfacial bonding between the steel substrate and TMC layers, an approximately 200 nm thick metallic titanium (Ti) interlayer was deposited. The deposition was carried out for 5 minutes with the DC power of 150 W in all three different TMC multilayers. Moreover, for multilayer TMC deposition, a fixed DC discharge power 150 W and deposition time of 60 minutes were used. In total, 12 alternate TMC layers (6 bilayer) were deposited in each multilayer with the individual layer duration of 5 minutes.

2.2 Coatings characterization

The crystallography of the TMC multilayer was analyzed by the GIXRD (Rigaku, Smart Lab) technique, using Cu K α radiation ($\lambda = 1.5406$ Å) with the incident angle and step size of 5° and 0.02°,

respectively. The lattice parameter (a) was calculated using the following equation,²⁰

$$a = \frac{\lambda \sqrt{h^2 + k^2 + l^2}}{2 \sin \theta} \quad (1)$$

where, λ is the X-ray wavelength, h , k and l are the miller indices of the planes and θ is the diffraction angle (in radians). The micro strain (ϵ) was determined using the following relation,²¹

$$\epsilon = \frac{\beta \cos \theta}{4} \quad (2)$$

where, β is the full width half maximum (FWHM) of the peaks. Moreover, the crystalline size (D) of TMC coatings was calculated using the Debye-Scherrer formula,

$$D = \frac{0.9\lambda}{\beta \cos \theta} \quad (3)$$

The FE-SEM (Carl Zeiss) technique was used to analyze the surface morphology and cross-section of the multilayer samples. EDAX elemental line profile analysis was utilized to study the compositional analysis of a cross-section of the samples. Confocal Raman microscope (Alpha 300 R, WITec) was used to probe the structural characteristics of the coated surface and wear track. Spectral information with the resolution of 1 cm^{-1} was obtained, using 1800 mm^{-1} grating at an excitation wavelength of 532 nm. The Raman spectrum was collected using a spectrometer equipped with a CCD camera coupled to a high-performance computer and software control system. The surface features were observed using a non-contact mode AFM (XE-70, Park Systems) analysis. Tribological properties of the samples against 100Cr6 steel balls (6 mm diameter) were studied using the linear reciprocating mode of a ball-on-disc microtribometer (CSM Instruments, Switzerland) under dry sliding conditions. The ball of 100Cr6 steel is widely used in bearing materials and used in a variety of mechanical applications. In thermal modified condition, this steel does not lose the mechanical properties mainly its hardness and resistance to abrasion, which are particularly suitable for wear resistance applications. In addition, 100Cr6 steel has high tensile strength and fatigue strength. The tribology test was conducted at room temperature (24 °C) under normal relative humidity (58%) condition. The total sliding time for tribology experiment to cover the 500 m was 7.28 hours. The calculated Hertz contact stress was 0.6, 0.72 and 0.76 GPa for TiC/CrC, TiC/ZrC and TiC/WC coatings, respectively. For each measurement, the sliding speed and applied load was kept constant about 3 cm s^{-1} and 1 N, respectively. The wear loss of the samples after the friction test was evaluated using a profilometer (Dektak XT Stylus profiler, Bruker) measuring the profile of the wear tracks. Nano-mechanical properties were measured by a Nanoindenter (Hysitron Troboidentor TI950, USA) using a Berkovich diamond indenter with the tip curvature radius of 150 nm. The maximum load of 9000 μN was applied to the indenter for this measurement. The loading-unloading range of $1500 \mu\text{N min}^{-1}$ was used for all the measurements. The load-displacement

curves were used to calculate the hardness (H) and reduced elastic modulus (E_r) of the coatings using Oliver–Pharr's method.²² The wear scar morphologies on the coatings and balls were observed by FE-SEM and optical microscope, respectively. The chemical changes in the wear track after tribological measurements were studied using Raman spectroscopy and EDAX elemental profile analysis.

3. Results and discussion

3.1 GIXRD analysis

The GIXRD diffraction patterns of the different TMC multilayer coatings deposited on steel substrates are shown in Fig. 1. In order to compare the results with single layers deposited under similar conditions, the diffraction patterns of single layer TMC coatings are also plotted in Fig. 1(a–d). The result shows multiple reflections of the TMC phases, indicating the polycrystalline nature of coatings. However, there are no obvious peaks observed for the chromium compounds in single layer CrC and multilayer TiC/CrC coatings (Fig. 1(b)), indicating the poor crystalline nature of CrC. Several earlier studies also reported the formation of amorphous/poor crystalline Cr-C phases in sputtered chromium carbide coatings.^{23–25} In all the multilayer samples, cubic TiC phases of (111), (200), (220) and (311) orientations were observed corresponding to the peak positions at 36°, 41.7°, 60.7° and 72.2°, respectively. These peaks are well matched with the single layer TiC coatings deposited under similar conditions, which are having the NaCl type FCC structure (JCPDS file no.: 71-0298), as shown in Fig. 1(a).

Similarly, FCC ZrC phase (JCPDS file no.: 35-0784) of (111), (200), (220) and (311) orientations was obtained at 32.8°, 38.2°,

55.1° and 65.9°, respectively, in the ZrC and TiC/ZrC coatings (Fig. 1(c)). The similar crystallography of the TiC and ZrC phases keeps them closely relative to each other (*i.e.* fewer lattice mismatch ratio between TiC and ZrC phases), in such a way that the TiC base layer facilitates ad-atoms mobility, initial nucleation and grain growth of the ZrC over layer and *vice versa*.²⁶ Meanwhile, the carbon atoms occupy the interstitial sites of Ti/Zr lattices, resulting in the formation of NaCl type FCC-TiC and ZrC structures. In the case of single layer WC and TiC/WC multilayer coatings (Fig. 1(d)), the observed diffraction peaks of (100), (202) and (220) orientations belong to the hexagonal W_2C phase (JCPDS file no.: 79-0743). In addition, the atomic radius of W is lower than that of the Ti atoms, due to which the W atoms migrated into the TiC crystalline sites, lead to the formation of a solid solution at the interface in TiC/WC multilayer coating. This phenomenon is explained from the peak broadening and relative shift of the peak positions centred at 39.3° and 72.5°. This is shown in Fig. 1(d).

From Fig. 1(c) and (d), the primary characteristic peaks of ZrC (111) and W_2C ($\bar{1}\bar{1}1$) orientations were obtained in the TiC/ZrC and TiC/WC coatings, followed by the secondary characteristic of the TiC (111) plane. The TiC (111) orientation dominates in the TiC/CrC multilayer, indicating poor crystalline nature of CrC layers (Fig. 1(b)). Due to the minimum surface and strain energy, the texture of (111) and (100) plane dominates. Therefore, these planes possess higher potential energy and cavitation diffusivities to dominate the texture.²² Moreover, relatively broader peaks with lower intensities were obtained for the TMC multilayer coatings as compared to the TMC single layers (Fig. 1). This indicates the confinement of the TMC crystallization/grain growth due to the limitations of the individual TMC layer thickness.

The calculated lattice parameter (a), micro strain (ϵ) and crystallite size (D) of different TMC phases presented in the multilayer are given in Table 1. In all the samples, lattice parameters of the different TMC phases except CrC were found to be slightly lower than those of standard data. This implies the presence of compressive stress in the TMC crystallites in all the multilayer coatings. Furthermore, the formation of the compressive stress is due to the thickness limitation along with the Z-direction of the alternate TMC layers.

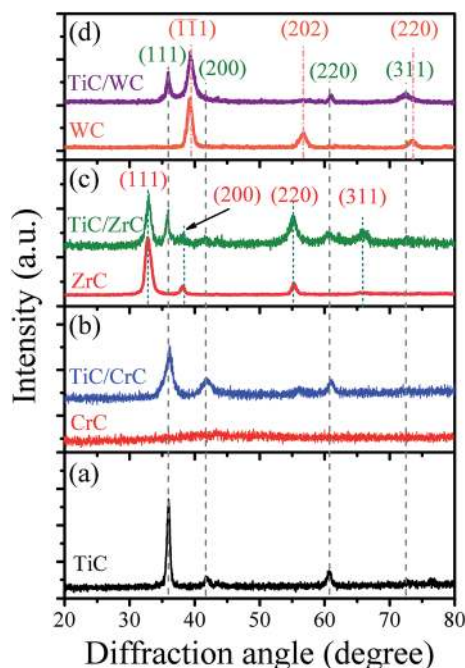


Fig. 1 GIXRD patterns of single layer and multilayer TMC coatings.

Table 1 Lattice parameter (a), micro strain (ϵ) and crystallite sizes (D) of the TMC multilayer coatings calculated from GIXRD results

| Sample | Phase | Lattice parameter, a (Å) | | | Crystallite size, D (nm) |
|---------|--------|----------------------------|------------|--------------------------|----------------------------|
| | | From JCPDS data | Calculated | Micro strain, ϵ | |
| TiC/CrC | TiC | 4.328 | 4.127 | 4.8×10^{-2} | 7.5 ± 1 |
| | CrC | — | — | — | — |
| TiC/ZrC | TiC | 4.328 | 4.231 | 2.3×10^{-2} | 18.3 ± 2 |
| | ZrC | 4.634 | 4.576 | 1.2×10^{-2} | 13.4 ± 2 |
| TiC/WC | TiC | 4.328 | 4.219 | 2.6×10^{-2} | 17.5 ± 2 |
| | W_2C | 5.190 | 4.928 | 4.3×10^{-2} | 10.2 ± 2 |

3.2 FE-SEM and EDAX analysis

The plane-view and cross-sectional view of FE-SEM images, with the corresponding EDAX elemental profile analysis of TiC/CrC, TiC/ZrC and TiC/WC multilayer coatings are shown in Fig. 2(a–c). The EDAX profile discloses that the transition metals and carbon elements were majorly present in the multilayer with 1 : 1 ratio. The Ti interlayer is clearly seen in the cross-sectional image (Fig. 2(a_{ii}–c_{ii})). This interlayer would promote the nucleation of TiC phases in all the multilayer coatings. The TiC/CrC multilayer consisted of cauliflower-like surface features due to the agglomeration of smaller adjacent crystallites. These structures were extended as the columnar growth of CrC layers, which can be obviously seen in the cross-sectional image (Fig. 2(a_{ii})). It has been reported that the columnar growth was formed for sputtered chromium compound coatings even at room temperature.^{27,28} However, in the case of TiC/ZrC multilayer, spherical topped and non-columnar/glassy structure was obtained, which might be due to the close crystallographic behaviour between the TiC and ZrC layers. Herein, the interface

between these two layers might be acting as pinning sites of the alternate layers, and hence, non-columnar grain growth, as shown in Fig. 2(b_{ii}).

Highly crystalline grains were formed on the TiC/CrC and TiC/ZrC coatings whereas, slightly lower crystallinity was attained in the TiC/WC multilayer. The lower atomic mobility and the crystallization potential of WC crystallites might be the reason for the decrease in the grain growth. In addition to this, the sharp interfaces between the different TMC layers indicate high degree of periodicity in the TiC/CrC and TiC/ZrC multilayer. EDAX elemental profile clearly supports this evidence and the results are shown in Fig. 2(a_{iii}) and (b_{iii}). However, the periodicity could not be observed in the TiC/WC samples due to the solid solution of TiC and WC layers at the interface during the deposition process. The EDAX profile emphasized the alloying of materials each other and therefore, the mixed phase was observed in the TiC/WC coating, as shown in Fig. 2(c_{iii}). This result is similar to the crystallography of this sample as obtained from the GIXRD analysis. Total coating thickness

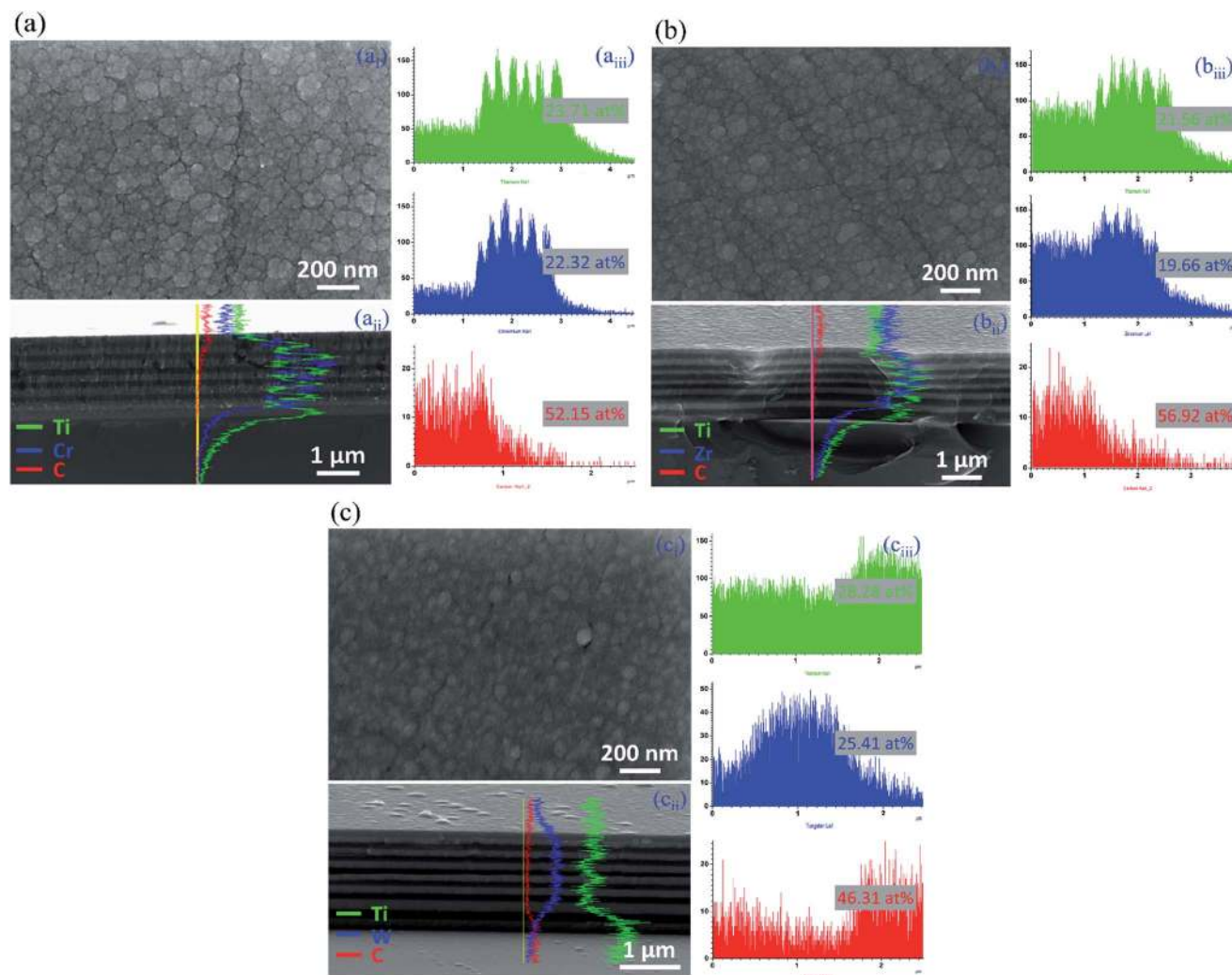


Fig. 2 FESEM and EDAX line profile analysis of (a) TiC/CrC, (b) TiC/ZrC and (c) TiC/WC multilayer. (a_i)–(c_i) surface morphology, (a_{ii})–(c_{ii}) cross-section and (a_{iii})–(c_{iii}) EDAX line profile analysis.

including the interlayer was found to be 2.2, 2.0 and 1.9 μm for the TiC/CrC, TiC/ZrC and TiC/WC samples, respectively. The individual thickness of the TiC layer was 160 nm, whereas, it varied as 175, 150 and 120 nm for the CrC, ZrC and WC layers, respectively. Herein, the variations in ad-atom mobility and reaction potential due to the different atomic mass of the transition metals tend to change in the deposition rate followed by the discrepancies in different layer thicknesses.²⁹

3.3 Raman analysis

In order to evaluate the chemical nature of the TMC multilayer, the coatings were characterized using Raman spectroscopy, as shown in Fig. 3(a–c). Raman vibrations are not active in stoichiometric TMC due to its inversion symmetry.³⁰ However, the Raman vibrational modes appeared in all the TMC multilayer samples, which are possibly activated by the carbon lattice vacancies and defects. Generally, sputtered coatings are known to possess several microscopic defects, followed by reduction of TMC crystallites symmetry.³¹ From Fig. 3(a–c), the peaks observed in the low-frequency range of 200–400 cm^{-1} correspond to the acoustic branches. The peaks obtained in the mid-frequency range of 630 cm^{-1} are due to the acoustic and optical branches of the TMC compounds. The peak positions centred at 274, 295, 342 and 356 cm^{-1} in Fig. 3(a) and (c), and 281 cm^{-1} in Fig. 3(b) indicate the near-stoichiometric TiC and ZrC, respectively.^{31,32} These results are well-attributed to the NaCl type TiC and ZrC crystalline structures as observed from the GIXRD results.

The peak position at 630 cm^{-1} represents the Raman active vibrational modes corresponding to the presence of the TiC phases. The Raman vibrational modes could not be anticipated

from the CrC and WC phases as shown in Fig. 3(b) and (c). This is related to the poor crystalline nature of CrC, and non-stoichiometric phase of WC (Fig. 1). Moreover, the excess amount of carbon atoms accumulated on the grain boundaries of TMC crystallites in the form of amorphous and disordered sp^2 bonding nature, which would increase the surface defects on the crystalline boundaries. The two peaks were obtained with nominal intensities corresponding to the D (1320 cm^{-1}) and G bands (1560 cm^{-1}) of disordered sp^2 carbons.¹⁶ This is shown in Fig. 3(a–c).

3.4 AFM analysis

The 3D and 2D surface topographies ($2.5 \times 2.5 \mu\text{m}$) of different TMC multilayer coatings with corresponding roughness are shown in Fig. 4. The surface features reveal the respective top layers of CrC, ZrC and WC in different multilayer coatings (Fig. 4(a)–(c)). The uniform distribution and spherical shaped particles were observed in all the samples, which are in good agreement with the FE-SEM results. The particle size was found to be higher (120 ± 30) nm for the TiC/CrC sample (Fig. 4(a)), whereas, it was lower for the TiC/ZrC (80 ± 20 nm) and TiC/WC (50 ± 10 nm) coatings (Fig. 4(b) and (c)).

These particles consisted of nano-sized grains, which could be due to the agglomeration of neighbouring grains with lower superficial energy, and it forms larger particles with a higher superficial energy.³³ The change in grain size is related to the grain boundary migration across the crystalline matrix. Mobility of the grain boundary and subsequent driving forces would raise the rate of grain growth, and therefore, different grain sizes were obtained in different TMCs under similar deposition conditions.³⁴ In addition, the 2D images showed amorphous structures around the grain boundaries. The excess amount of carbon atoms may occupy the grain boundaries of the crystalline matrix, and it obstructs the grain size and smoothing effect of TMC multilayer. Based on these grain size variations, the surface roughness also varied for the different multilayer.

3.5 Tribo-mechanical properties

Tribological properties of different TMC multilayer coatings deposited on 316LN steel substrates were studied by a micro-tribometer, using 100Cr6 steel ball as a sliding counter body. The tribological behaviour of an uncoated substrate under similar conditions has been reported elsewhere.³⁵

3.5.1 Frictional behaviour. The average friction coefficient values of the single layer and multilayer TMC coatings sliding under similar conditions are shown in Fig. 5. The friction curves are provided in the ESI data (Fig. S1 and S2†). In single layers, the friction coefficient was lowest ~ 0.21 in TiC and highest ~ 0.98 in WC coatings. Intermediate values were obtained for the CrC (0.5) and ZrC (0.42) coatings. The value was almost similar in the TMC multilayer coatings (Fig. 5(b–d)). Lower standard deviation and steady-state friction curves were obtained in the TiC/CrC and TiC/ZrC multilayer samples (Fig. S1†). In these cases, initially low friction values were attained for a few sliding cycles, and then they saturated up to

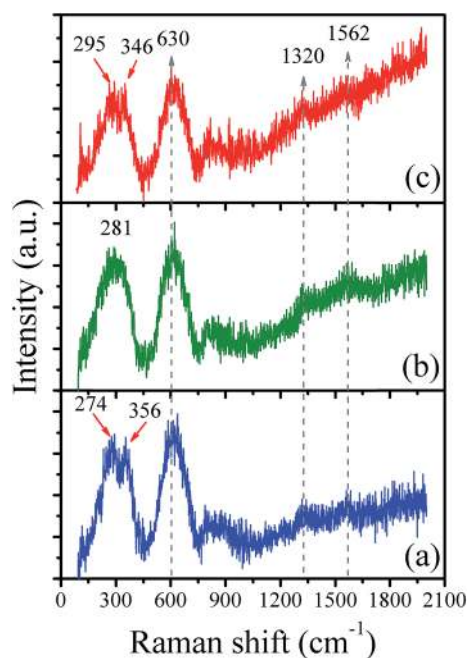


Fig. 3 Raman spectra of (a) TiC/CrC, (b) TiC/ZrC and (c) TiC/WC multilayer.

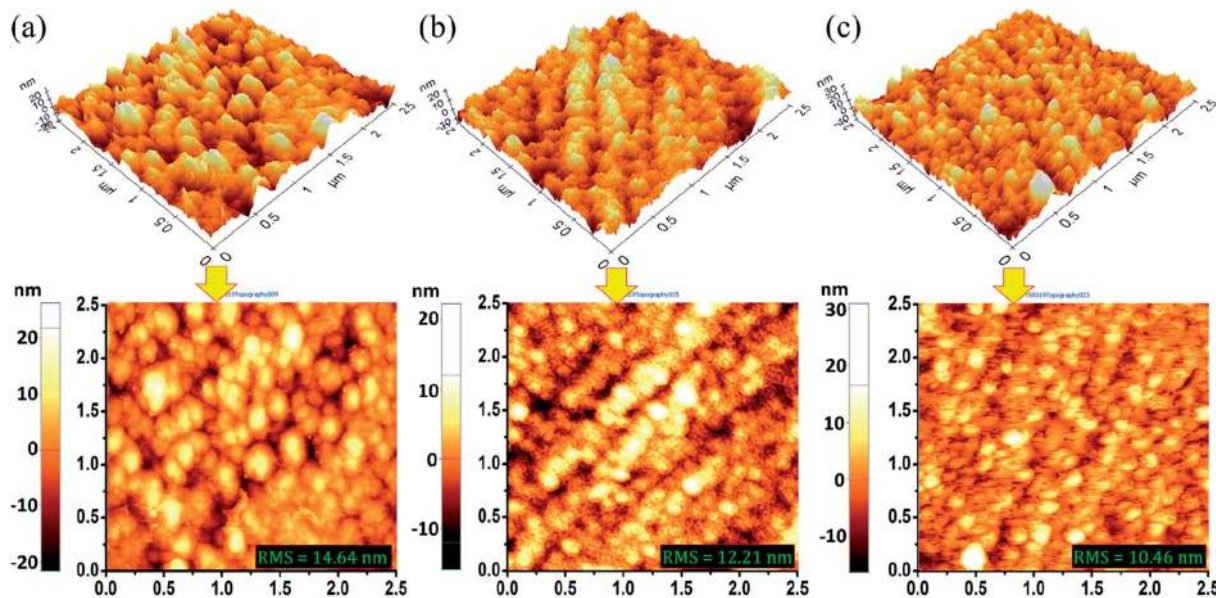


Fig. 4 2D and 3D AFM topographies of (a) TiC/CrC, (b) TiC/ZrC and (c) TiC/WC multilayer coatings.

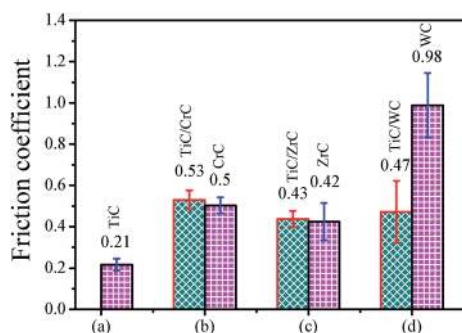


Fig. 5 Friction coefficient values of different single layer and multilayer TMC coatings.

500 m of sliding distance. A tribolayer of sp^2 hybridized amorphous carbons (a-C) accumulated on these surfaces, which would constantly tend to decrease the friction initially (Fig. S1(a) and (b)†).^{16,36} After a few sliding cycles, the carbon layers break down and friction increases due to the wear loss. The standard deviation was quite higher in the TiC/WC sample (Fig. 5(d)) and this might have originated from the WC layer. The friction coefficient was much higher in the TiC/WC coating up to 80 m of sliding distance, and on further increasing the sliding distance, it significantly decreases to a lower value of 0.4 (Fig. S1(c)†).

3.5.2 Wear behaviour. Wear profiles of the coatings after the tribological test were measured using Dektak profiler, and the average wear depths of the single layer and multilayer TMC coatings are shown in Fig. 6. Significantly higher wear and more damage occurred on the wear track of the single layer CrC and WC samples (Fig. S4(b) and (d)†), whereas, lower wear was obtained on the TiC and ZrC samples (Fig. S4(a) and (c)†). Even though the friction was slightly higher in multilayer than

single layer coatings, the wear resistance was significantly improved. Fig. 7 shows the FE-SEM images of the wear track of the TMC multilayer. The inset optical images in Fig. 7 showed the sliding ball scar, denoting the contact area and wear scar morphology. From the wear profile and FE-SEM results, it can be estimated that three different mechanisms were involved in the wear behaviour for three different coatings. The abrasive wear mode dominates the wear behaviour in the TiC/CrC sample, while adhesive wear dominates in the TiC/ZrC, and, both abrasive and adhesive wear governed in the TiC/WC sample.

The wear rate was calculated using the following equation,¹⁶

$$k(\text{mm}^3 \text{N}^{-1} \text{m}^{-1}) = V/F_n \times S \quad (4)$$

where, k is the wear rate, V is the wear volume, F_n is the normal applied load and S is the sliding distance. The magnitude of wear rate was found to be higher ($4.7 \times 10^{-5} \text{mm}^3 \text{N}^{-1} \text{m}^{-1}$) on the TiC/CrC coating, whereas, it was extremely low ($2.1 \times 10^{-8} \text{mm}^3 \text{N}^{-1} \text{m}^{-1}$) in the TiC/ZrC sample. The intermediate wear

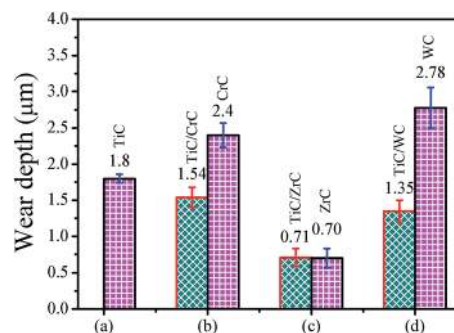


Fig. 6 Wear depth of different single layer and multilayer TMC coatings after tribological measurements.

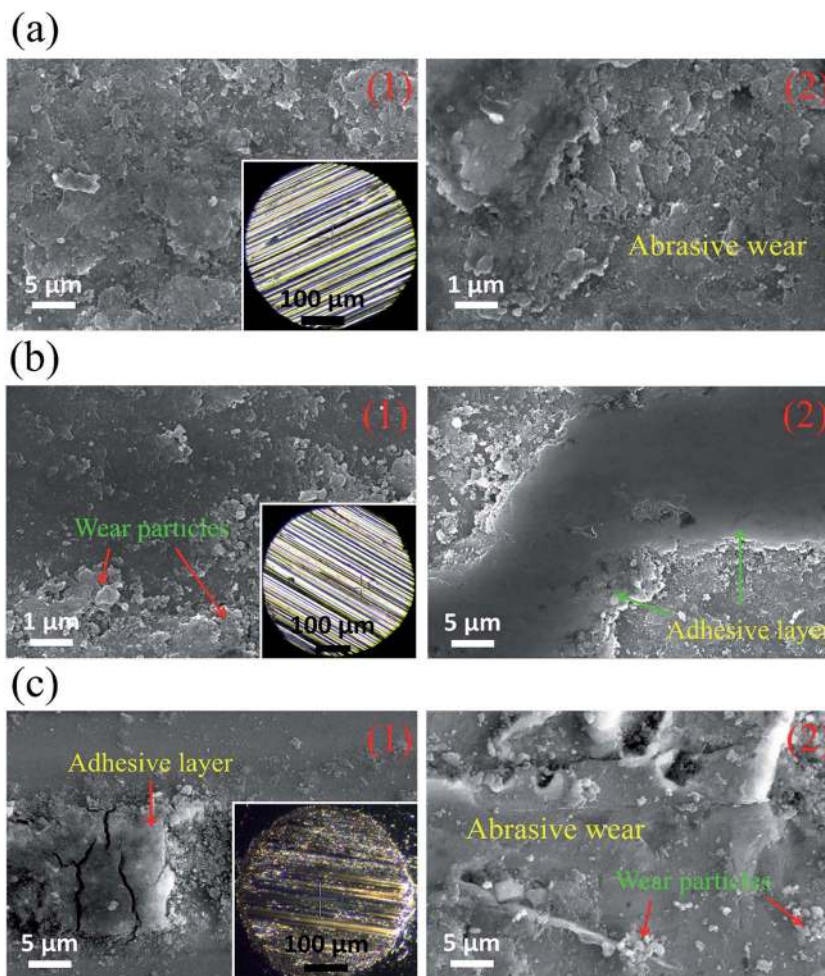


Fig. 7 FE-SEM micrographs of the wear tracks on (a) TiC/CrC, (b) TiC/ZrC and (c) TiC/WC multilayer.

rate observed in the TiC/WC multilayer was about $7.6 \times 10^{-6} \text{ mm}^3 \text{ N}^{-1} \text{ m}^{-1}$. The wear rates of single layer TMC coatings are given in Table S1.†

3.5.3 Tribological mechanism. The complete tribological process between two different contact surfaces is complex, because of the various factors simultaneously involved in the tribological measurements. Those are, friction, wear, deformation and material transfer mechanisms from nano to micro scale.^{37,38} On the other hand, tribological behavior of the TMC multilayer could be explained in terms of microstructure and mechanical properties.^{9,39} FESEM images (Fig. 7(a)) showed severe deformation of the coating and ball wear in sliding against TiC/CrC multilayer. Wear depth analysis also well-established that significantly higher wear takes place in this sample, as illustrated in Fig. 6(a). Fig. 8 shows the nano-mechanical properties of multilayer coatings. The higher penetration depth depicts that the TiC/CrC sample exhibited poor hardness ($H = 17.1 \pm 2 \text{ GPa}$) and weak elastic modulus ($E = 224.9 \pm 7 \text{ GPa}$). Therefore, a weak resistance to plastic deformation (H^3/E^2) (0.098 GPa) was attained, which increases the deformation of coating plastically during indentation as well as tribological measurements. Reduced tribo-mechanical

properties were due to the poor crystalline nature (from GIXRD result) and columnar growth of CrC layers (as seen from the FE-SEM analysis), which easily nucleate and expanding the cracks under stress leading to a lower fracture toughness. It is a well-known factor that the higher oxidation resistance of chromium compounds would enhance the friction as well as wear.⁴⁰

In the TiC/ZrC sample, the adhesive wear mode dominates the tribological behaviour. Wear dimension was comparatively lower in this sample, as shown in Fig. S3(b).† Moreover, FE-SEM image shows the transferred layers from ball materials noticeably deposited over the coating surface. Due to the higher contact stress and frictional heat, wear of the coating gradually took place during the initial sliding passes; later, the oxidized ball material transferred onto the coating surface. A similar behaviour was obtained in the previous observations of the steel ball sliding against the ZrN coating.³⁵ Because of the lower electronegativity and thermal expansion coefficient of the Zr atoms, the ball material (iron) was bonded with Zr and formed adhesive layers. Besides, improved nanomechanical properties were also obtained for the TiC/ZrC multilayer, as shown in Fig. 8(b). The fine-grained structure and (111) preferred

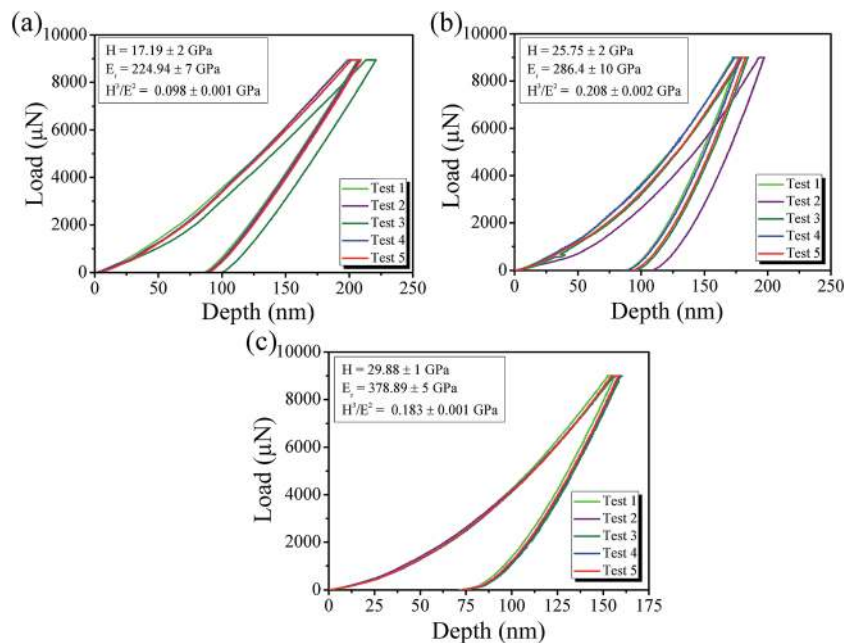


Fig. 8 Nanoindentation results of (a) TiC/CrC, (b) TiC/ZrC and (c) TiC/WC multilayer coatings.

orientations of TiC and ZrC crystalline phases would enhance the mechanical properties ($H = 25.7 \pm 2$ GPa, $E = 276.4 \pm 10$ GPa and $H^3/E^2 = 0.208$ GPa). Since, the (111) orientation has zero Schmid factor in all the slip planes owing to a higher packing density than other orientations.⁴¹ Because of the preferred orientation and oxidized lubrication layers, the friction coefficient was significantly decreased followed by enhanced wear resistance.⁴²

Unlike other samples, the initial wear loss was exceptionally high in the TiC/WC coating, which displays the sudden increase of wear depth, as shown in Fig. 6(c). Improved nanomechanical properties ($H = 29.88 \pm 1$ GPa, $E = 378.8 \pm 5$ GPa and $H^3/E^2 = 0.183$ GPa) were attained in this sample, and this is primarily related to the ultra-fine grain. Moreover, the solid solution of the TiC and WC layers at the interfaces would also resist the plastic deformation during indentation, and the subsequent lower penetration depth, as displayed in Fig. 8(c). Initially, the contact stress was higher due to the less contact area, and it would enhance the wear dimension abruptly. On further increasing the sliding cycles, the contact stress decreases and contact area increases; this tends to saturate the wear behaviour.^{35,36,43} On the other hand, the wear profile illustrates the severe deformation of the coating material, which might be related to third body interaction (Fig. S4(d)†). In general, the abrasive/detached wear particles from the ball, as well as the TMC layers might be trapped at the sliding interface.⁴⁴ During continuous sliding, the concentration of defect complex increases, which enhanced the strain hardening of these wear particles, resulting in deep scratches inside the wear track. The FE-SEM image in Fig. 7(c) shows the presence of deep grooves and ploughing of particulates in the wear track, which obviously trapped/crushed hard particles. However, the friction value was found to be lower in this

sample (Fig. 5(c)), which might be due to the oxidation of the deposited third bodies.

3.5.4 Chemical changes in the wear track. In order to elucidate the tribo-physical and tribo-chemical changes, the worn surface was characterized using Raman spectroscopy and the results are shown in Fig. 9. The inset images in Fig. 9 represent the optical micrographs corresponding to the Raman analysis on different locations of the wear track. Three different locations were analyzed in each sample, such as near the edge of the wear track (location 1), centre of the wear track (location 2) and deformation zones (location 3). From these spectrums, it can be assessed that the peaks at the higher-frequency region ($1300\text{--}1600\text{ cm}^{-1}$), mid-frequency region ($400\text{--}800\text{ cm}^{-1}$) and lower-frequency region ($200\text{--}400\text{ cm}^{-1}$) correspond to the Raman bands of sp^2 carbons (D and G bands), TMC phases and metal-oxide phases, respectively.^{16,32,43,45}

The intensities of disordered sp^2 carbons (D bands between $1319\text{--}1343\text{ cm}^{-1}$ and G bands between $1561\text{--}1570\text{ cm}^{-1}$) in all the samples (Fig. 9(a–c)) are significantly higher near the edge (location 1) than at the coating surface (Fig. 3(a–c)) as well as locations 2 and 3. The higher kinetic friction force at the center of the wear track drives the sp^2 carbons towards the edge, and hence, amorphous carbons were accumulated at location 1. Herein, two possible simultaneous mechanisms are involved in the formation of the sp^2 carbons. Firstly, out diffusion of carbon atoms from the TMC crystallites, and secondly, higher chemical reactions between the transition metals and ambient atmosphere. Moreover, these bands are shifted towards higher optical phonon vibrations compared to the surface (D band at 1319 cm^{-1} and G band at 1560 cm^{-1}), due to the mechanical alloying of steel ball and sp^2 carbons.^{16,32} Since, these carbons are highly inactive to the chemical reactions under normal conditions. Similarly, the Raman peaks of the TiC phase in all

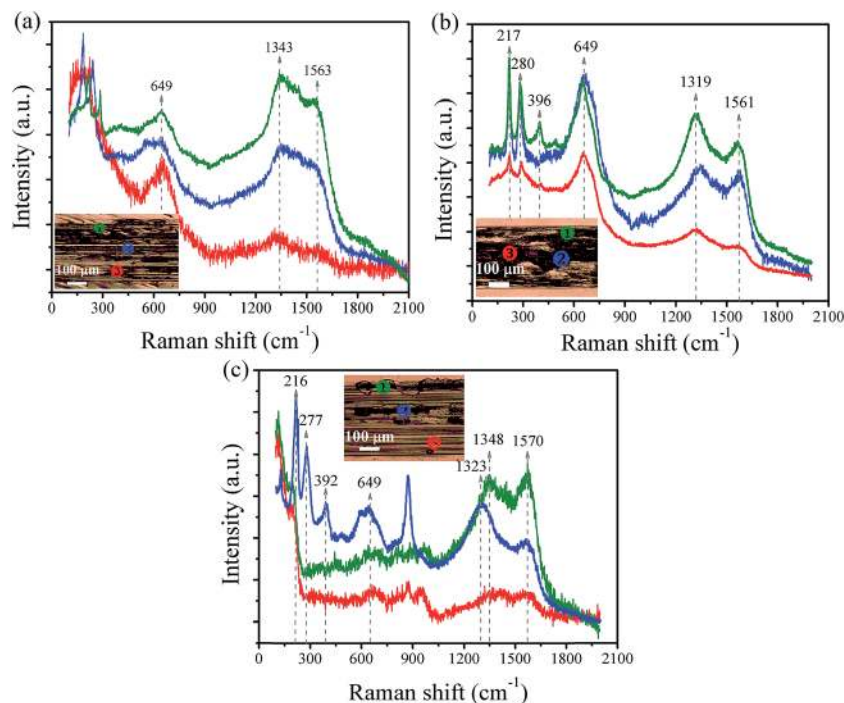


Fig. 9 Raman spectra analysis inside the wear track of (a) TiC/CrC, (b) TiC/ZrC and (c) TiC/WC multilayer coatings.

the samples shifted towards the higher-frequency region 649 cm^{-1} (Fig. 9) as compared to the surface 630 cm^{-1} (Fig. 3). This shift is related to the increase of lattice strain and defect concentration, due to the high flash temperature and contact stress.¹⁶ Owing to the higher wear resistance of the TiC/ZrC coating and severe adhesive wear behavior of the steel ball, the intensity of the TiC phase was almost similar in all the three different locations, as shown in Fig. 9(b). Instead, this trend was not followed in the TiC/CrC and TiC/WC coatings because of the abrasive wear behavior followed by the lower wear resistance of coatings. Therefore, the intensity of the TiC phase (649 cm^{-1}) was diminished in these samples at locations 2 and 3, as illustrated in Fig. 9(b) and (c).

The peaks obtained at low-frequency regions ($200\text{--}300\text{ cm}^{-1}$) in all the samples were expected from the acoustic vibrations of metal-oxides (oxidized iron), which are obviously transferred from the sliding steel counter body.^{46,47} The lower intensity and broader metal-oxide peaks in TiC/CrC sample are related to severe abrasive wear. This is discussed in Section 3.5.3. In other samples (*i.e.* TiC/ZrC and TiC/WC), these metal-oxide peaks dominated, which ensures the transfer of materials to the wear tracks.

Specifically, these peaks were dominant in TiC/ZrC in all the three different locations (Fig. 9(b)). This could be due to the severe adhesive behaviour of the steel ball on the TiC/ZrC multilayer, followed by the improvement in lubricity and wear resistance. Owing to the combined effect of the abrasive and adhesive wear behaviour, the TiC/WC coating exhibited intermediate wear resistance. The microstructure dependent friction mechanism and tribo-chemical changes of different TMC multilayer coatings are schematically shown in Fig. 10(a–c).

Chemical compositions obtained from the EDAX analysis (Fig. S7(a–c)†) are remarkable evidence of the formation of various elements inside the wear tracks; this is well-supported by the Raman spectroscopy results.

3.6 Motivation

The present work aims to reveal the comparison of the tribo-mechanical properties of single layer and multilayer TMC coatings. The larger crystalline domains in single layer coatings facilitate the propagation of plastic deformation along the orientations during tribo-mechanical contact. Thus, the plastically deformed zone increases, which develops the loose wear particles/debris at the sliding interface. In this condition, the required mechanical energy is minimum and hence, there is lower friction but higher wear. Grain refinement is the key parameter in the TMC multilayer to enhance the mechanical properties and wear resistance than single layers. In fine-grained structures, grain rotation and grain boundary sliding are the major governing factors of plastic deformation during tribo-mechanical contact, which increases the strain energy of the coatings.³⁸ Therefore, more mechanical energy is required to plastically deform the coatings across the interface of different TMC layers, having different shear modulus, and thus, it increases the friction and decreases the wear. Moreover, these interfaces would act as a reservoir of plastic energy, which inhibits plastic deformation. The change in crystalline nature on varying the TMC layers, could also be the reason for the enhancement of the tribo-mechanical properties in the multilayer. However, an extremely hard multilayer may produce a large amount of strain energy against plastic

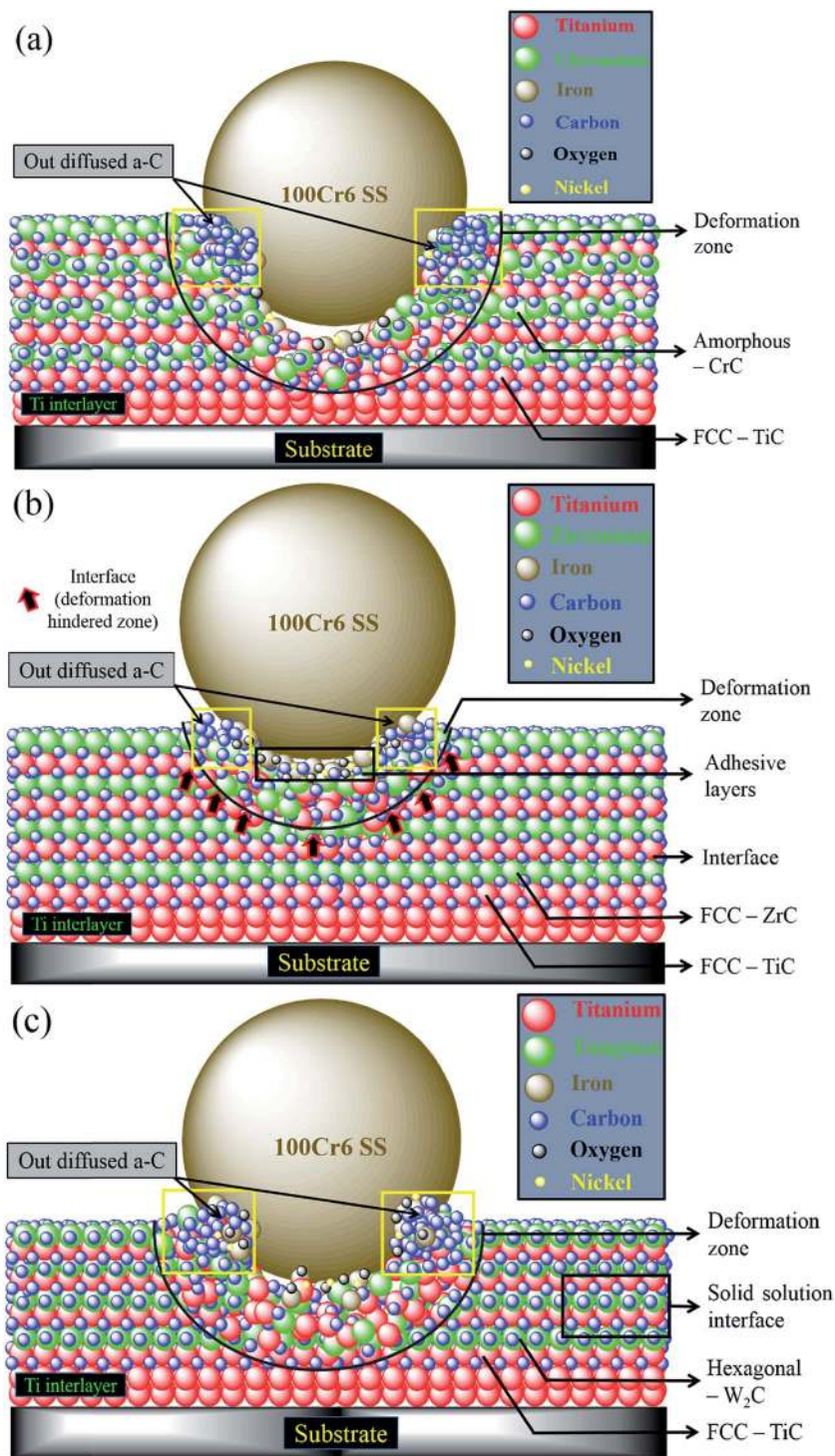


Fig. 10 Friction model of TMC multilayer coatings (a) TiC/CrC, (b) TiC/ZrC and (c) TiC/WC.

deformation during tribological contact, resulting in coating delamination. In this work, mechanical properties of TMC multilayer coatings are intermediate and therefore, no delamination occurs in TMC multilayer coatings. Such improved properties of coatings are typically controlled by the deposition conditions.

4. Conclusion

TiC/CrC, TiC/ZrC and TiC/WC multilayer coatings were deposited on 316LN steel substrates by the reactive DC magnetron sputtering technique. Additionally, the TMC single layer (TiC, CrC, ZrC and WC) coatings deposited under similar conditions were also studied to compare the tribo-mechanical properties of

the TMC multilayer. The FE-SEM results revealed that the well-defined periodic multilayer was formed in TiC/CrC and TiC/ZrC coatings with the non-columnar growth of TiC and ZrC, except CrC layers. A high friction coefficient of 0.53 and higher wear rate of $4.7 \times 10^{-5} \text{ mm}^3 \text{ N}^{-1} \text{ m}^{-1}$ were observed in the TiC/CrC coating. Such characteristics originated from poor crystallinity and lower mechanical properties, which enhance the severe abrasive wear. However, enhanced tribo-mechanical properties were obtained in the TiC/ZrC sample, due to the improved microstructure and H^3/E^2 values. In this case, friction coefficient reduced to 0.42 and wear resistance highly increased to $2.1 \times 10^{-8} \text{ mm}^3 \text{ N}^{-1} \text{ m}^{-1}$, when adhesive wear mode dominated. The presence of higher compressive stress and preferred (111) crystalline orientations served to enhance the tribo-mechanical characteristics of the TiC/ZrC multilayer.

Conflict of interest

The authors declare that there is no competing financial interest.

Acknowledgements

D. Dinesh Kumar gratefully acknowledges the Council of Scientific and Industrial Research (CSIR), Government of India, for awarding a Senior Research Fellowship (SRF), Sanction no.: 09/468(460)/2012-EMR-I. The authors would like to thank the CSIR, Government of India, for providing financial support to carry out this research work (CSIR project Sanction order no. 03(1266)/12/EMR-II).

References

- 1 S. J. Zinkle and G. S. Was, *Acta Mater.*, 2013, **61**, 735–758.
- 2 M. Talha, C. K. Behera and O. P. Sinha, *Mater. Sci. Eng.*, C, 2013, **33**, 3563–3575.
- 3 A. Devaraju, A. Elaya Perumal, J. Alphonsa, S. V. Kailas and S. Venugopal, *Wear*, 2012, **288**, 17–26.
- 4 S. C. Tjong and H. Chen, *Mater. Sci. Eng.*, R, 2004, **45**, 1–88.
- 5 J. Xu, X. Zhao, P. Munroe and Z. Xie, *Sci. Rep.*, 2014, **4**(4239), 1–8.
- 6 L. Yate, L. Emerson Coy, G. Wang, M. Beltran, E. Diaz-Barriga, E. M. Saucedo, M. A. Cenicerros, K. Załęski, I. Llarena, M. Moller and R. F. Ziolo, *RSC Adv.*, 2014, **4**, 61355–61362.
- 7 D. W. Flaherty, N. T. Hahn, D. Ferrer, T. R. Engstrom, P. L. Tanaka and C. Buddie Mullins, *J. Phys. Chem. C*, 2009, **113**(29), 12742–12752.
- 8 M. Kot, Ł. Major, K. Chronowska-Przywara, J. M. Lackner, W. Waldhauser and W. Rakowski, *Mater. Des.*, 2014, **56**, 981–989.
- 9 E. Lewin, B. Andr, S. Urbonaite, U. Wiklund and U. Jansson, *J. Mater. Chem.*, 2010, **20**, 5950–5960.
- 10 V. Khetan, N. Valle, D. Duday, C. Michotte, C. Mitterer, M.-P. Delplancke-Ogletree and P. Choquet, *ACS Appl. Mater. Interfaces*, 2014, **6**, 15403–15411.
- 11 L. Major, J. M. Lackner and B. Major, *RSC Adv.*, 2014, **4**, 21108–21114.
- 12 G. S. Fox-Rabinovich, K. Yamamoto, B. D. Beake, I. S. Gershman, A. I. Kovalev, S. C. Veldhuis, M. H. Aguirre, G. Dosbaeva and J. L. Endrino, *Sci. Technol. Adv. Mater.*, 2012, **13**, 043001.
- 13 N. Dwivedi, S. Kumar and H. K. Malik, *ACS Appl. Mater. Interfaces*, 2011, **3**, 4268–4278.
- 14 M. Kot, Ł. Major and J. Lackner, *Mater. Des.*, 2013, **51**, 280–286.
- 15 P.-L. Sun, C.-Y. Su, T.-P. Liou, C.-H. Hsu and C.-K. Lin, *J. Alloys Compd.*, 2011, **509**, 3197–3201.
- 16 N. Kumar, G. Natarajan, R. Dumpala, R. Pandian, A. Bahuguna, S. K. Srivastava, T. R. Ravindran, S. Rajagopalan, S. Dash, A. K. Tyagi and M. S. Ramachandra Rao, *Surf. Coat. Technol.*, 2014, **258**, 557–565.
- 17 L. Major, M. Janusz, M. Kot, J. M. Lackner and B. Major, *RSC Adv.*, 2015, **5**, 9405–9415.
- 18 M. T. P. McCann, D. A. Mooney, M. Rahman, D. P. Dowling and J. M. Don MacElroy, *ACS Appl. Mater. Interfaces*, 2011, **3**, 252–260.
- 19 D. K. Devarajan, K. Sivakumar and J. Ramasamy, *Mater. Express*, 2014, **4**, 453–464.
- 20 S. Heiroth, R. Frison, J. L. M. Rupp, T. Lippert, E. J. Barthazy Meier, E. M. Gubler, M. Döbeli, K. Conder, A. Wokaun and L. J. Gauckler, *Solid State Ionics*, 2011, **191**, 12–23.
- 21 B. Subramanian, K. Ashok, G. Selvan, V. Senthil Kumar and M. Jayachandran, *Surf. Eng.*, 2010, **26**, 555–561.
- 22 W. C. Oliver and G. M. Pharr, *J. Mater. Res.*, 1992, **7**, 1564–1583.
- 23 M. Magnuson, M. Andersson, J. Lu, L. Hultman and U. Jansson, *J. Phys.: Condens. Matter*, 2012, **24**, 225004.
- 24 S. Sen, *Mater. Des.*, 2006, **27**, 85–91.
- 25 G. Gassner, P. H. Mayrhofer, C. Mitterer and J. Kiefer, *Surf. Coat. Technol.*, 2005, **200**, 1147–1150.
- 26 J. C. Caicedo, C. Amayaa, L. Yate, O. Nos, M. E. Gomez and P. Prieto, *Mater. Sci. Eng.*, B, 2010, **171**, 56–61.
- 27 T. Elangovan, P. Kuppasami, R. Thirumurugesan, V. Ganesan, E. Mohandas and D. Mangalaraj, *Mater. Sci. Eng.*, B, 2010, **167**, 17–25.
- 28 K. H. Thulasi Raman, M. S. R. N. Kiran, U. Ramamurty and G. Mohan Rao, *Mater. Res. Bull.*, 2012, **47**, 4463–4466.
- 29 R. Pandey, B. K. Rao, P. Jena and M. A. Blanco, *J. Am. Chem. Soc.*, 2001, **123**, 3799–3808.
- 30 K. J. Cai, Y. Zheng, P. Shen and S. Y. Chen, *CrystEngComm*, 2014, **16**, 5466–5474.
- 31 H. C. Barshilia and K. S. Rajam, *J. Mater. Res.*, 2004, **19**(11), 3196–3205.
- 32 S. Pellegrino, L. Thomé, A. Debelle, S. Miro and P. Trocellier, *Nucl. Instrum. Methods Phys. Res., Sect. B*, 2014, **327**, 103–107.
- 33 D. Arias, A. Devia and J. Velez, *Surf. Coat. Technol.*, 2010, **204**, 2999–3003.
- 34 P. H. Mayrhofer, H. Willmann and C. Mitterer, *Thin Solid Films*, 2003, **440**, 174–179.
- 35 D. Dinesh Kumar, N. Kumar, S. Kalaiselvam, S. Dash and R. Jayavel, *Ceram. Int.*, 2015, **41**, 9849–9861.

- 36 A. A. C. Recco, C. C. Viáfara, A. Sinatora and A. P. Tschiptschin, *Wear*, 2009, **267**, 1146–1152.
- 37 G. W. Rowe, *R. Inst. Chem., Rev.*, 1968, **1**, 135–204.
- 38 D. Dinesh Kumar, N. Kumar, S. Kalaiselvam, S. Dash and R. Jayavel, *Tribol. Int.*, 2015, **88**, 25–30.
- 39 S. Zhou, L. Wang, Z. Lu, Q. Ding, S. C. Wang, R. J. K. Wood and Q. Xue, *J. Mater. Chem.*, 2012, **22**, 15782–15792.
- 40 Y. H. Cheng, T. Browne and B. Heckerman, *Wear*, 2011, **271**, 775–782.
- 41 J.-H. Huang, K.-W. Lau and G.-P. Yu, *Surf. Coat. Technol.*, 2005, **191**, 17–24.
- 42 X. Yu, X. Zhao, Y. Liu, M. Hua and X. Jiang, *ACS Appl. Mater. Interfaces*, 2014, **6**, 4669–4677.
- 43 O. Smerdova, D. Mazuyer and J. Cayer-Barrioz, *Tribol. Int.*, 2014, **77**, 148–159.
- 44 M. Andersson, J. Högström, S. Urbonaite, A. Furlan, L. Nyholm and U. Jansson, *Vacuum*, 2012, **86**, 1408–1416.
- 45 P. Stoyanov, P. Stemmer, T. T. Jarvi, R. Merz, P. A. Romero, M. Scherge, M. Kopnarski, M. Moseler, A. Fischer and M. Dienwiebel, *ACS Appl. Mater. Interfaces*, 2013, **5**, 6123–6135.
- 46 Q. Luo, S. Cai Wang, Z. Zhou and L. Chen, *J. Mater. Chem.*, 2011, **21**, 9746–9756.
- 47 T. Polcar, F. Gustavsson, T. Thersleff, S. Jacobson and A. Cavaleiro, *Faraday Discuss.*, 2012, **156**, 383–401.